A Hybrid CPT System Using Quadrature Double Horizontal Capacitive Couplers for High-Misalignment Tolerance and Constant Voltage Output

Ting Chen, Zhihui Ma, Zhicheng Xu, Fengxian Wang, Xian Zhang, Guangyao Li, Xuan Zhao,
and Yuqiao Wang

***Abstract*—In capacitive power transfer (CPT) systems, coupling variations are inevitable due to air gap changes and misalignment between transmitting and receiving plates, which hinders constant output and optimal efficiency. This article proposes a hybrid CPT system using quadrature double horizontal capacitive couplers for high-misalignment tolerance and constant voltage (CV) output. The system employs a hybrid compensation topology that combines *LCLC-LC* and *LC-LCLC* compensation topologies, based on structure of input-parallel-output-series. QDHCC serve as the power transfer channels, achieving decoupling as the coupler moves along the *X*, *Y*, and *Z* axes. This design mitigates complex cross-couplings and ensures independence between the two power transfer channels. A triple-effect multiobjective optimization method for compensation circuit parameters is proposed to further enhance the system's tolerance to misalignment, reduce the voltage stress on the coupler and improve system efficiency. The CV output within predetermined misalignment distance is obtained. The alignment tolerance for adjustments along the *X*-axis and *Y*-axis is 40%, while it reaches 100% for the *Z*-axis. Finally, experimental results demonstrated the effectiveness of the proposed scheme with a maximum efficiency of 87.5%.**

***Index Terms*—Capacitive power transfer (CPT), constant voltage (CV), high tolerance, hybrid topologies, plate misalignment, quadrature Double horizontal capacitive couplers (QDHCC), triple-effect multiobjective optimization method.**

I. INTRODUCTION

NEAR-FIELD wireless power transfer can be categorized into capacitive power transfer (CPT) and inductive power transfer (IPT). Compared to IPT, CPT has merits, such as lower cost, lighter weight, better tolerance to misalignment, and no eddy current heating effects when metal is near the capacitive coupler. In practical applications, such as consumer electronics [1], electric vehicle charging [2], automated guided vehicle [3], uncrewed aerial vehicle [4], coupler misalignment is unavoidable between transmitter and receiver, which results in output instability and reduction in system efficiency. Moreover, the overvoltage and overcurrent caused by misalignment may exceed the rated limits of the circuit components, potentially deteriorating the system, especially in cleaning scenarios—such as office buildings, solar panels, underground pipelines and high-rise buildings with glass facades—where large operating areas and multiple charging places are required. Furthermore, these systems are typically expected to operate autonomously, imposing strict demands on misalignment tolerance to maintain stable charging. Therefore, this article focuses on enhancing the misalignment tolerance in cleaning robot applications.

To enhance tolerance to misalignment, existing methods can be classified into three categories: control scheme, capacitive coupler design and topology parameter optimization. In terms of control strategies, Lu et al. [5] adopted frequency tuning in the inverter to achieve constant voltage (CV) output. Xue et al. [6] employed pulse frequency modulation to enable flexible adjustment of the output voltage. Qing et al. [7] simultaneously combined frequency tracking and phase shift control to mitigate the effect of coupler misalignment and load variation on system output. Although the abovementioned methods effectively reduce output fluctuations, frequency bifurcation tends to exist and additional converters need to cascade to realize zero phase angle (ZPA) [8]. An alternative method is to maintain a stable mutual capacitance against misalignment. The basic idea is to design a capacitive coupler array that aligns sequentially during misalignment to maintain a stable coupling area [9],

Received 27 June 2025; revised 4 September 2025; accepted 19 September 2025. Date of publication 26 September 2025; date of current version 23 December 2025. This work was supported in part by the National Natural Science Foundation of China under Project 52307009, Project 52122701, and Project 52477005, in part by Hebei Province Yan Zhao Golden Terrace Talent Gathering Plan Key Talent Project under Grant B2024011, in part by the State Key Laboratory of Reliability and Intelligence of Electrical Equipment under Grant EERI_OY2023001, in part by the Key Program of Natural Science Foundation of Tianjin under Grant 22JCZDJC00620, in part by the Hebei Provincial Central Guidance Local Science and Technology Development Project 236Z5201G, in part by the Hebei Yanzhao Young Scientist Project E2024202109, in part by the S&T Program of Hebei under Grant 24464401D, and in part by the Continuation Funding Project for Innovative Research Groups of Natural Science Foundation of Hebei Province E2024202298. Recommended for publication by Associate Editor M. P.-Silva. *(Corresponding author: Xian Zhang.)*

The authors are with the State Key Laboratory of Intelligent Power Distribution Equipment and System, Hebei University of Technology, Tianjin 300401, China, and also with the Hebei Key Laboratory of Equipment and Technology Demonstration of Flexible DC Transmission, Hebei University of Technology, Tianjin 300401, China (e-mail: tingchen@hebut.edu.cn; 202321401107@stu.hebut.edu.cn; xzc@hebut.edu.cn; 202111401013@stu.hebut.edu.cn; zhangxian@hebut.edu.cn; 202221401084@stu.hebut.edu.cn; 202211401015@stu.hebut.edu.cn; 202331402008@stu.hebut.edu.cn).

Color versions of one or more figures in this article are available at https://doi.org/10.1109/TPEL.2025.3614976.

Digital Object Identifier 10.1109/TPEL.2025.3614976

which avoids the control complexity. Li et al. [10] introduced a circular capacitive coupler with multilayer interleaving to mitigate the misalignment issue, enhancing self-couplings and reducing cross-couplings. Mutual capacitance stabilization is achieved by maintaining the projection area of the receiving plates aligned with that of the transmitting plates. Liang et al. [11] incorporated switches to dynamically align the transmitting plates with the moving receiving plates, thereby stabilizing the coupling coefficient when misaligned. However, system cost increases. Besides, the large transmitter area increases electric field radiation and reduces system efficiency. To reduce the complexity of the capacitive coupler, optimizing compensation circuit parameters can also improve the system antimisalignment capability. For instance, Qing et al. [12] optimized the parameters of a bilateral *LC*-compensated network to maintain the required constant output voltage coupling capacitance. However, the system only achieves misalignment tolerance in the *X*-direction. Luo et al. [13] proposed an *LC*-*CLC* compensation network capable of delivering constant power output in both the *X*- and *Y*- directions. However, it suffers significant power fluctuations within a large misalignment range.

As a duality of the CPT system, some works in IPT system combines two compensation topologies with opposite trends in output variation when coil alignment is mismatched. The opposing variation in output voltage/ current /power enables the total output to remain constant over a certain range of coupling variations. Typical examples of CV output include the parallel combination of the *LCC*-*LCC* and SS topologies in [14], as well as the series transmitter and parallel receiver combinations of *LCC*-S and S-*LCC* topologies in [16] and [19], respectively. Zhao et al. [15] superposed *LCC*-*LCC* and SS topologies in series on both sides to realize constant power output. Chen et al. [17] adopted *LCC*-S and S-*LCC* topologies in parallel on the transmitter and in series on the receiver. To ensure independent power transfer between the two basic topologies, the magnetic field decoupling between two power transfer channel is necessary. For example, hybrid DD pad [14], double-D-quadrature [16], [17], bipolar pad [18] and quadruple-D-quadrature pad [19] are employed. The aforementioned hybrid topologies provide an effective solution for misalignment tolerance, which has the merits of not requiring complex control circuits and can maintain high robustness against misalignment, exhibiting low output fluctuations over wide variations of coupling coefficient.

However, due to the complex cross-coupling between the plates in the CPT system, the resonance and power transfer performance will be significantly affected under misalignment. The superstition of two topologies with opposite characteristics against misalignment cannot ease the variation of the total output. In order to achieve power decoupling between two power transfer channels, Chen et al. [20] proposed a decoupling relay unit by rotating the receiver by 90° relative to the transmitter, ensuring equal facing areas between the transmitting and receiving plates in a horizontal coupler configuration. However, this method is only applicable to long-distance wireless charging systems with relay units. When misalignment occurs in the receiver of the two power transfer channels, the decoupling performance of the relay unit degrades, resulting in system detuning. Zhou et al. [21] introduced a decoupling circuit based on shared inductors, which resonates with the mutual capacitances on the same side of the coupler, thereby eliminating cross-couplings that disrupt system resonance. However, under capacitive coupler misalignment, the shared inductors need to be adjusted in real-time according to the displacement of the capacitive coupler. This results in necessitating additional detection and control circuits. Thus, the capacitive coupler structure design for high misalignment tolerance is a better option.

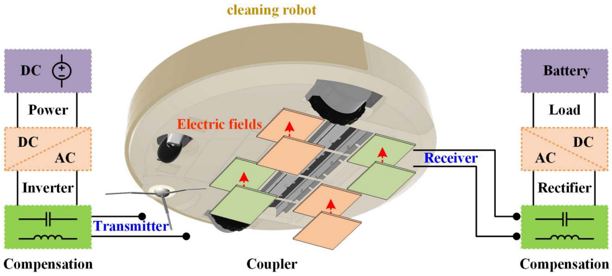

Fig. 1. Structure of the proposed hybrid CPT system applied to cleaning robot.

To ensure the independence of the two main power transfer channels and realize CV output under capacitive coupler misalignment, this article proposes a hybrid system with high tolerance to plate misalignment and CV output. The main contributions of this article are as follows.

1) A novel hybrid configuration of the *LCLC*-*LC* and *LC*-*LCLC* topologies is proposed to achieve CV output for the CPT system, based on the structure of input-parallel-output-series (IPOS). This hybrid topology also enhances tolerance to misalignment.
2) Quadrature double horizontal capacitive coupler (QDHCC) featuring decoupling is proposed and modeled for cleaning robot, capable of eliminating the cross-coupling and same-side coupling during misalignment between plates, thus enabling independent power transfer in the two electric field transmission channels.
3) A triple-effect multiobjective optimization method for compensation capacitances is proposed, which reduces the voltage stress on the coupler, improves system efficiency and enhances misalignment tolerance. The system achieves CV output when the plates are misaligned by 40% along the *X*-axis and the *Y*-axis, and 100% along the *Z*-axis with a load of 100 Ω.

The rest of this article is organized as follows. The proposed hybrid topology is presented and analyzed in Section II. Section III presents the decoupling characteristics of the QDHCC. The parameter optimization approach is analyzed in Section IV. The experimental verification is offered and a comparison with similar hybrid topologies in Section V. Finally, Section VI concludes the article.

II. PROPOSED HYBRID *LCLC*-*LC* AND *LC*-*LCLC* COMPENSATION TOPOLOGIES

The structure of the proposed hybrid CPT system applied to the cleaning robot is shown in Fig. 1. The corresponding

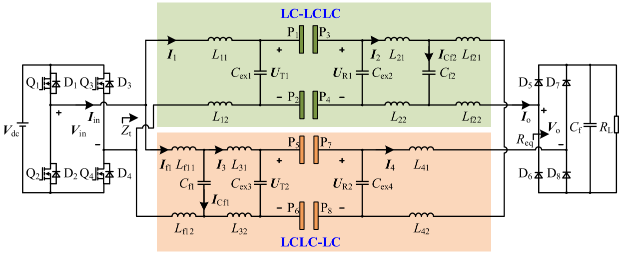

Fig. 2. Hybrid compensation topology of *LCLC-LC* and *LC-LCLC* with IPOS.

circuit topology, namely the proposed *LC-LCLC* and *LCLC-LC*-based hybrid CPT topology for CV output in IPOS structure, is depicted in Fig. 2. A dc voltage V_{dc} is inverted by a full bridge, generating a square wave voltage that serves as the input on the primary side. The upper resonant circuit employs an *LC-LCLC* compensation topology, while the lower side adopts an LCLC-LC topology. The secondary resonant circuit outputs are connected to the diode rectifier. The *LC-LCLC* topology include L_{11}, L_{12}, C_{ex1}, C_{ex2}, L_{21}, L_{22}, C_{f2}, L_{f21}, and L_{f22}, which are used to compensate the capacitive reactance among plates P_1, P_2, P_3, and P_4. The *LCLC-LC* topology consists of L_{f11}, L_{f12}, C_{f1}, L_{31}, L_{32}, C_{ex3}, C_{ex4}, L_{41}, and L_{42}, which are adopted to compensate the capacitive reactance among plates P_5, P_6, P_7, and P_8. The function of the *LC-LCLC* network is to decrease the output voltage when the plate misalignment occurs, and the function of the *LCLC-LC* network is to increase the output voltage when the plate misalignment occurs. Two topologies having opposite trends in output variation with plate misalignment shows complementary characteristics, which can be used to achieve a constant output within a wide range of coupling variation. To simplify the subsequent theoretical analysis, the external capacitors C_{ex1}, C_{ex2}, C_{ex3}, and C_{ex4} are assumed to be equal and are all denoted as C_{ex}. To simplify the coupler with complex capacitive couplings into multiple two-port networks for analysis, split inductors are employed to ensure that the currents into and out of each of the four plates are equal, thereby guaranteeing the two-port characteristics [22]. Accordingly, compensation inductances should satisfy the following equations: $L_{11} = L_{12}$, $L_{21} = L_{22}$; $L_{f21} = L_{f22}$; $L_{f11} = L_{f12}$; $L_{31} = L_{32}$; and $L_{41} = L_{42}$.

Fig. 3 illustrates the equivalent induced voltage source (IVS) model of the proposed system. Due to the band-pass characteristic of the proposed system, the fundamental harmonics approximation method is adopted for circuit analysis. V_{in} is the fundamental component of the inverter output voltage. The full-bridge rectifier with a real load R_L is regarded as resistive and can be modeled as a load resistance R_{eq} [19]. C_1, C_2, C_3, and C_4 represent the equivalent self-capacitances of the coupler. C_{pm} and C_{vm} denote mutual capacitances of the two main power transfer channels. C_{mm} and C_{qm} represent the same-side coupling capacitances. C_{nm} and C_{km} represent the cross-coupling capacitances. L_1 denotes the equivalent inductor of the splitting inductors L_{11} and L_{12}, where $L_1 = L_{11} + L_{12}$. Similarly, $L_2 = L_{21} + L_{22}$, $L_3 = L_{31} + L_{32}$, $L_4 = L_{41} + L_{42}$, $L_{f1} = L_{f11} + L_{f22}$, and $L_{f2} = L_{f21} + L_{f22}$. The parasitic resistances of each branch are denoted as r_1, r_2, r_3, r_4, and r_5. According to Kirchhoff voltage law (KVL), the mathematical model with the CV output can be expressed as

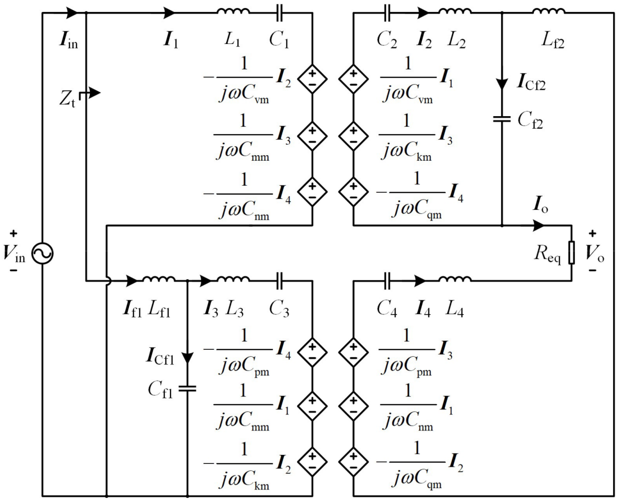

Fig. 3. IVS model of the proposed system.

$$\begin{cases} I_1X_1 - I_2X_{Cvm} + I_3X_{Cmm} - I_4X_{Cnm} = V_{\mathrm{in}} \\ -I_1X_{Cvm} + I_2(X_2 + X_{\mathrm{Cf2}}) \\ -I_3X_{Ckm} + I_4X_{Cqm} + I_{\mathrm{o}}X_{Cf2} = 0 \\ I_{Lf1}(X_{Lf1} + X_{Cf1}) - I_3X_{Cf1} = V_{\mathrm{in}} \\ I_1X_{Cmm} - I_2X_{Ckm} + I_3(X_{Cf1} + X_3) \\ -I_4X_{Cpm} - I_{Lf1}X_{\mathrm{Cf1}} = 0 \\ -I_1X_{Cnm} + I_2(X_{Cqm} - X_{\mathrm{Cf}Cf22}) - I_3X_{Cpm} \\ -I_{\mathrm{o}}(X_4 + X_{Cf2} + X_{Lf2}) = V_o \end{cases} \tag{1}$$

where $X_1 = j\omega L_1 + 1/(j\omega C_1)$, $X_2 = j\omega L_2 + 1/(j\omega C_2)$, $X_3 = j\omega L_3 + 1/(j\omega C_3)$, $X_4 = j\omega L_4 + 1/(j\omega C_4)$, $X_{Cf1} = 1/(j\omega C_{f1})$, $X_{Lf1} = j\omega L_{f1}$, $X_{Cf2} = 1/(j\omega C_{f2})$, $X_{Lf2} = j\omega L_{f2}$, $X_{Cvm} = 1/(j\omega C_{vm})$, $X_{Cpm} = 1/(j\omega C_{pm})$, $X_{Cmm} = 1/j\omega C_{mm}$, $X_{Cnm} = 1/j\omega C_{nm}$, $X_{Ckm} = 1/j\omega C_{km}$, $X_{Cqm} = 1/j\omega C_{qm}$. I_1, I_2, I_3, I_4, and I_{f1} denote the currents flowing through each branch. V_o and I_{o} represent the load voltage and current, respectively.

In order to achieve input ZPA and CV output with high misalignment tolerance, the system works at the resonant angular frequency ω_0. The resonant conditions are using the following equations:

$$\begin{cases} \omega_0^2 L_1C_1 = \omega_0^2 L_{f2}C_{f2} = \omega_0^2 L_2C_2C_{f2}/(C_2 + C_{f2}) = 1 \\ \omega_0^2 L_4C_4 = \omega_0^2 L_{f1}C_{f1} = \omega_0^2 L_3C_3C_{f1}/(C_3 + C_{f1}) = 1. \end{cases} \tag{2}$$

It should be noted that the diagonally configured plate pairs are employed as the capacitive coupler to eliminate the same-side coupling C_{mm}, C_{qm} and cross-coupling C_{nm}, C_{km} between the plates, which will be analyzed in the design of the capacitive couplers in Section III. In this case, the energy transfer characteristics of the system depend solely on the main coupling capacitances C_{pm} and C_{vm}. Thus, after solving (1) and (2), the

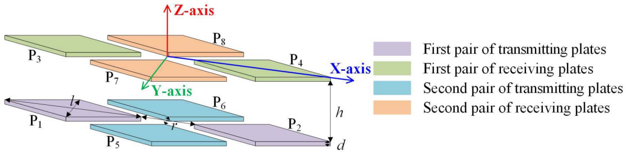

Fig. 4. Structure of proposed QDHCC.

currents in each branch can be yielded as

$$\begin{cases} I_1 = \frac{C_{vm}V_o}{C_{f2}R_{\text{eq}}}, I_{Lf1} = \frac{C_{f1}V_o}{C_{pm}R_{\text{eq}}} \\ I_2 = -j\omega_0 C_{vm}V_{\text{in}}, I_3 = -j\omega_0 C_{f1}V_{\text{in}} \\ I_{Cf1} = \frac{C_{f1}V_o}{C_{pm}R_{\text{eq}}} + j\omega_0 C_{f1}V_{\text{in}}, I_{Cf2} = \frac{V_o}{R_{\text{eq}}} - j\omega_0 C_{vm}V_{\text{in}} \\ I_4 = -I_{\text{o}} = -\frac{V_o}{R_{\text{eq}}} \end{cases}. \tag{3}$$

The ideal output voltage gain E_{t} can be derived as

$$E_t = \frac{V_{\text{o}}}{V_{\text{in}}} = \frac{C_{vm}}{C_{f\mathbf{2}}} + \frac{C_{f\mathbf{1}}}{C_{pm}}. \tag{4}$$

It can be seen from (4) that the output voltage gain of the hybrid structure has no relation with the load. The influence of same side coupling and cross-coupling is ignored. The voltage gain is positively correlated with C_{vm} and is negatively correlated with C_{pm}. The main mutual capacitances (C_{vm} and C_{pm}) exhibit the same variation trend under misalignment in this article. If main mutual capacitances decrease (or increase) with misalignment, C_{vm}/C_{f2} will decrease (or increase) while C_{f1}/C_{pm} will increase (or decrease). As a result, given the properly designed parameters, the sum of C_{vm}/C_{f2} and C_{f1}/C_{pm} can remain relatively constant within a predetermined misalignment distance. Hereinafter, the sum of C_{vm}/C_{f2} and C_{f1}/C_{pm} is defined as the E_t in this article, i.e., $E_t = C_{vm}/C_{f2} + C_{f1}/C_{pm}$.

Based on (3), the input impedance Z_t can be derived as

$$Z_t = \frac{V_{\text{in}}}{I_{\text{in}}} = \frac{V_{\text{in}}}{I_1 + I_{f1}} = \frac{R_{\text{eq}}}{E_t^2}. \tag{5}$$

It can be seen from (5) that ZPA is realized and the input impedance is only relevant to load resistance and voltage gain.

III. DECOUPLING DESIGN OF CAPACITIVE COUPLER UNDER ANTIMISALIGNMENT

The proposed QDHCC, illustrated in Fig. 4, consists of two sets of plates arranged diagonally to form two independent power transfer channels. One channel along the *X*-axis consists of transmitting plates P_1 and P_2, and receiving plates P_3 and P_4, the other channel along the *Y*-axis comprises transmitting plates P_5 and P_6 and receiving plates P_7 and P_8. All plates are identical in size. Since the system employs a hybrid compensation network with split inductors, the proposed capacitive coupler can be regarded as a superposition of six two-port networks. The equivalent self-capacitances and mutual capacitances can be expressed as

$$\begin{cases} C_1 = \frac{C_{\text{P1P2}}C_{\text{P3P4}} - C_{\text{M1234}}^2}{C_{\text{P3P4}}}, C_2 = \frac{C_{\text{P1P2}}C_{\text{P3P4}} - C_{\text{M1234}}^2}{C_{\text{P1P2}}} \\ C_3 = \frac{C_{\text{P5P6}}C_{\text{P7P8}} - C_{\text{M5678}}^2}{C_{\text{P7P8}}}, C_4 = \frac{C_{\text{P5P6}}C_{\text{P7P8}} - C_{\text{M5678}}^2}{C_{\text{P5P6}}} \\ C_{vm} = \frac{C_{\text{P1P2}}C_{\text{P3P4}} - C_{\text{M1234}}^2}{C_{\text{M1234}}}, C_{pm} = \frac{C_{\text{P5P6}}C_{\text{P7P8}} - C_{\text{M5678}}^2}{C_{\text{M5678}}} \end{cases} \tag{6}$$

where C_{M1234} and C_{M5678} can be represented by (7), and C_{P1P2}, C_{P3P4}, C_{P5P6}, and C_{P7P8} can be represented as

$$C_{\text{M}mnkq} = \frac{C_{mk} \times C_{nq} - C_{mq} \times C_{nk}}{C_{mk} + C_{mq} + C_{nk} + C_{nq}} \tag{7}$$

$$C_{PiPj} = C_{ij} + C_{\text{ex}j/2} + \frac{(C_{i3} + C_{i4}) \times (C_{j3} + C_{j4})}{C_{i3} + C_{i4} + C_{j3} + C_{j4}} + \frac{(C_{i5} + C_{i6}) \times (C_{j5} + C_{j6})}{C_{i5} + C_{i6} + C_{j5} + C_{j6}} + \frac{(C_{i7} + C_{i8}) \times (C_{j7} + C_{j8})}{C_{i7} + C_{i8} + C_{j7} + C_{j8}} \tag{8}$$

where C_{ij} is capacitance between any two plates P_i and P_j.

The mutual capacitance C_{mm}, C_{qm} between the same-side plates and the mutual capacitance C_{nm}, C_{km} between the cross-side plates can be expressed as

$$\begin{cases} C_{mm} = \frac{C_{\text{P1P2}} \times C_{\text{P5P6}} - C_{\text{M1256}} \times C_{\text{M1256}}}{C_{\text{M1256}}} \\ C_{qm} = \frac{C_{\text{P3P4}} \times C_{\text{P7P8}} - C_{\text{M3478}} \times C_{\text{M3478}}}{C_{\text{M3478}}} \\ C_{nm} = \frac{C_{\text{P1P2}} \times C_{\text{P7P8}} - C_{\text{M1278}} \times C_{\text{M1278}}}{C_{\text{M1278}}} \\ C_{km} = \frac{C_{\text{P3P4}} \times C_{\text{P5P6}} - C_{\text{M3456}} \times C_{\text{M3456}}}{C_{\text{M3456}}} \end{cases} \tag{9}$$

where C_{M1256}, C_{M1278}, C_{M3456}, and C_{M3478} can be represented by (7) [23].

Due to the symmetry of the coupler under misalignment, the capacitances of symmetrically positioned plates in the offset direction remain equal. For instance, $C_{17} = C_{18}$ and $C_{27} = C_{28}$ can be obtained when the receiver shifts along the *X*-axis. $C_{17} = C_{27}$ and $C_{18} = C_{28}$ can be obtained when the receiver shifts along the *Y*-axis. Moreover, $C_{17} = C_{18}$, $C_{27} = C_{28}$, $C_{17} = C_{27}$ and $C_{18} = C_{28}$ can be obtained when the receiver shifts along the *Z*-axis. As a result, $C_{\text{M1278}} = 0$ can be concluded by (7) when the receiver shifts along the *X*-axis, *Y*-axis, and *Z*-axis. Besides, C_{M1256}, C_{M3456} and C_{M3478} are both 0 by similar analysis, which indicates that the capacitance decoupling is achieved. Thus, when the capacitive coupler misaligns, the decoupling characteristics will remain intact as long as the symmetry of the capacitive coupler is maintained. Consequently, the proposed QDHCC in Fig. 4 achieves decoupling.

The finite-element analysis (FEA) is employed to verify the decoupling characteristics of the proposed capacitive coupler. The diagonal length *l* of the plate is 30 cm, the spacing *r* between plates on the same side is 30 cm, the thickness *d* of the plate is 2 mm, and the transmission distance *h* is 10 mm. Fig. 5 illustrates the mutual capacitance variations versus different *X*-axis, *Y*-axis, and *Z*-axis misalignments. Because the mutual capacitances C_{mm}, C_{nm}, C_{km}, and C_{qm} are infinite and cannot be directly represented in the figures, the capacitances C_{M1234}, C_{M5678}, C_{M1256}, C_{M1278}, C_{M3456}, and C_{M3478} are employed for analysis. Fig. 5 indicates that the capacitive coupler effectively

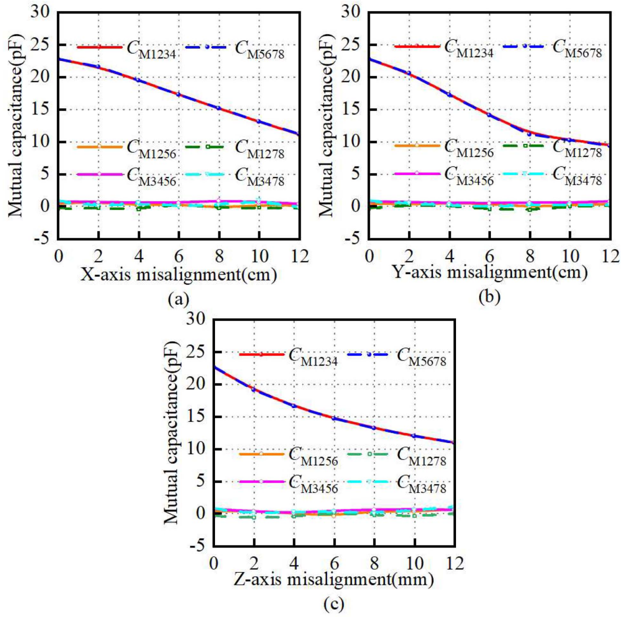

Fig. 5. Mutual capacitances varying with three directional misalignments. (a) *X*-axis misalignment. (b) *Y*-axis misalignment. (c) *Z*-axis misalignment.

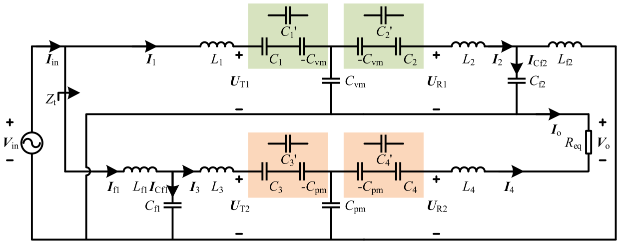

Fig. 6. Equivalent circuit of the proposed system with T-type network.

reduces C_{M1256}, C_{M1278}, C_{M3456}, and C_{M3478} to near zero. Thus, the proposed capacitive coupler not only eliminates the coupling between transmitting plates or receiving plates on the same side, but also eliminates the cross-coupling between nonopposite plates on the opposite side.

IV. TRIPLE-EFFECT MULTIOBJECTIVE OPTIMIZATION METHOD OF COMPENSATION PARAMETERS

A. *Voltage Stress*

According to the analysis in Section II-A, the IVS model of the proposed system shown in Fig. 3 is equivalent to a T-type network, as illustrated in Fig. 6. The equivalent capacitance C_1', C_2', C_3', and C_4' can be expressed as: C_1' = -C_1C_{vm}/(C_1-C_{vm}), C_2' = -C_2C_{vm}/(C_2-C_{vm}), C_3' = -C_3C_{pm}/(C_3-C_{pm}), C_4' = -C_4C_{pm}/(C_4-C_{pm}). U_{T1} and U_{R1} are the voltage stress across the primary plates and the secondary plates of the *LC-LCLC* topology. U_{T2} and U_{R2} are the voltage stress across the primary plates and the secondary plates of the *LCLC-LC* topology. The voltage stresses U_{T1}, U_{R1}, U_{T2}, and U_{R2} are marked in Figs. 2 and 6.

Based on (3) and (4), the voltage stress U_{R1}, U_{T1}, U_{R2}, and U_{T2} across the primary and the secondary side can be derived as

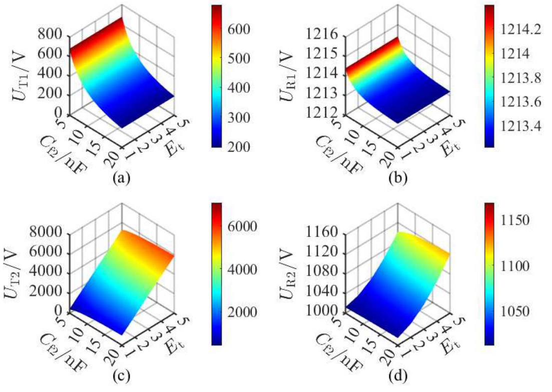

Fig. 7. Voltage stress versus varying C_{f2} and E_t.

$$\begin{cases} U_{T1} = \sqrt{V_{\text{in}}^2 + \frac{P_o^2}{k^2\omega_0^2 C_{f2}^2 E_t^2 V_{\text{in}}^2}} \\ U_{R1} = \sqrt{\frac{1}{k^2}V_{\text{in}}^2 + \frac{P_{\text{o}}^2}{\omega_0^2 C_{f2}^2 E_t^2 V_{\text{in}}^2}} \\ U_{T2} = \sqrt{\left(E_t - \frac{\sqrt{C_3C_4}}{kC_{f2}}\right)^2 \frac{V_{\text{in}}^2}{k^2} + \frac{P_o^2 k^2}{\omega_0^2 C_3^2 E_t^2 V_{\text{in}}^2}} \\ U_{R2} = \sqrt{\left(E_t - \frac{\sqrt{C_3C_4}}{kC_{f2}}\right)^2 V_{\text{in}}^2 + \frac{P_o^2}{\omega_0^2 C_4^2 E_t^2 V_{\text{in}}^2}} \end{cases} . \tag{10}$$

As shown in (10), U_{T1} and U_{R1} are influenced by coupling coefficient k, $C_{f2,}$ and E_t. It can be observed that the primary-side voltages U_{T1} and U_{T2} are influenced by C_{f2} and E_t, whereas the secondary-side voltages U_{R1} and U_{R2} remain relatively unaffected from Fig. 7. Moreover, U_{T2} is the maximum voltage stress, which demonstrates that reducing C_{f2} and E_t leads to a proportional decrease in voltage stress. The influence of E_t on voltage stress is significant. In contrast, the influence of C_{f2} on voltage stress is relatively small. Thus, E_t is first determined and $E_t = 1.7$ is selected to minimize the voltage stress across the coupling plates. The influence of coupling coefficient k on voltage stress will be analyzed in Section V.

B. *Optimal Efficiency*

The reactive power of the compensation inductor Q_1 can be expressed as

$$Q_1 = I_1^2\omega_0 L_1 + I_2^2\omega_0 L_2 + I_{f1}^2\omega_0 L_{f1} + I_3^2\omega_0 L_3 + I_o^2\omega_0 L_{f2} + I_o^2\omega_0 L_4. \tag{11}$$

The reactive power of the coupler Q_2 can be expressed as

$$Q_2 = I_1^2\frac{1}{\omega_0 C'_1} + I_2^2\frac{1}{\omega_0 C'_2} + I_3^2\frac{1}{\omega_0 C'_3} + I_o^2\frac{1}{\omega_0 C'_4} + |I_1 - I_2|^2\frac{1}{\omega_0 C_{vm}} + |I_3 - I_4|^2\frac{1}{\omega_0 C_{pm}}. \tag{12}$$

The reactive power of the compensation capacitor Q_3 can be expressed as

$$Q_3 = I_{Cf1}^2\frac{1}{\omega_0 C_{f1}} + I_{Cf2}^2\frac{1}{\omega_0 C_{f2}}. \tag{13}$$

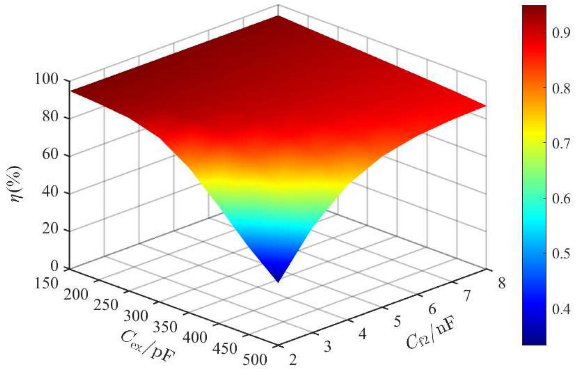

Fig. 8. Maximum efficiency versus varying C_{f2} and C_{ex}.

The system output power P can be expressed as

$$P = I_o^2 R_{\mathrm{eq}} = \frac{V_o^2}{R_{\mathrm{eq}}}. \tag{14}$$

Defining the quality factor of each inductor and capacitor as their reactive power to active power ratio. Based on (3), the system efficiency η can be expressed as

$$\eta = \frac{P}{P + \frac{Q_1}{Q_{\mathrm{L}}} + \frac{Q_2}{Q_{\mathrm{S}}} + \frac{Q_3}{Q_{\mathrm{C}}}} = \frac{1}{1 + T_1 + T_2} \tag{15}$$

where

$$\begin{cases} T_1 = \left(\frac{1}{Q_L C_1} + \frac{1}{Q_S C_1}\right)\left(\frac{C_{vm}^2 + C_{f2}^2}{\omega_0 R_{\mathrm{eq}} C_{f2}^2} + \frac{\omega_0 R_{\mathrm{eq}}(C_{vm}^2 + C_{f1}^2)}{E_t^2}\right) \\ T_2 = \left(\frac{1}{Q_L} + \frac{1}{Q_C}\right)\left(\frac{\omega_0 R_{\mathrm{eq}} C_{pm}}{E_t} + \frac{E_t}{\omega_0 R_{\mathrm{eq}} C_{pm}}\right) \end{cases} \tag{16}$$

where Q_L is the quality factor of the compensation inductor, Q_C is the quality factor of the compensation capacitor and Q_S is the quality factor of the capacitive coupler. By differentiating the efficiency with respect to the load, the optimal efficiency can be determined at the optimal load R_p

$$R_p = \sqrt{\frac{\left(\frac{1}{Q_{\mathrm{L}} C_1} + \frac{1}{Q_S C_1}\right)\frac{C_{pm}^2 + C_{f2}^2}{\omega_0 C_{f2}^2} + \left(\frac{1}{Q_L} + \frac{1}{Q_C}\right)\frac{E_t}{\omega_0 C_{pm}}}{\left(\frac{1}{Q_L C_1} + \frac{1}{Q_S C_1}\right)\frac{\omega_0\left(C_{pm}^2 + C_{f1}^2\right)}{E_t^2} + \left(\frac{1}{Q_L} + \frac{1}{Q_C}\right)\frac{\omega_0 C_{pm}}{E_t}}}. \tag{17}$$

Substituting (16) and (17) into (15), it is found that the maximum efficiency is related to C_1, C_{vm}, C_{pm}, E_t, C_{f2}, and C_{f1}. As analyzed in the previous section on voltage stress, E_t has been determined. C_1, C_{vm}, and C_{pm} are associated with the parallel capacitor C_{ex}. From (4), C_{f1} can be derived from C_{f2} and E_t. Therefore, the maximum efficiency mainly depends on C_{ex} and C_{f2}. The maximum efficiency variations with respect to C_{ex} and C_{f2} are illustrated in Fig. 8. As demonstrated, the optimal efficiency increases with decreasing C_{ex} and increasing C_{f2}. The influence of C_{f2} on system efficiency gradually weakens when C_{ex} decreases. Thus, $C_{\mathrm{ex}} = 250$ pF is selected to maximize the system efficiency.

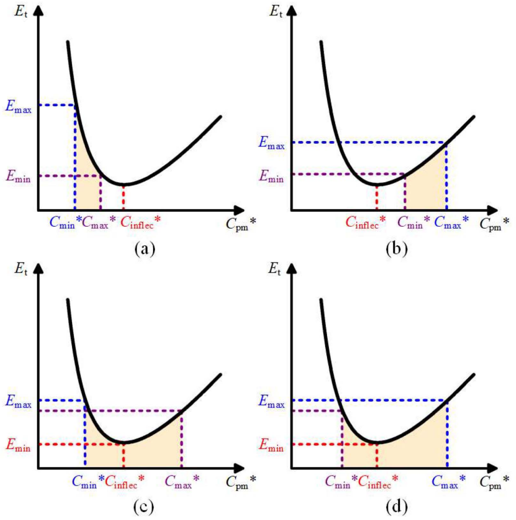

(a)

(b)

(c)

(d)

Fig. 9. Voltage gain E_t versus varying $C_{pm}*$. (a) $E_{\max} = f(C_{pm\min}*)$ &$E_{\min} = f(C_{pm\max}*)$. (b) $E_{\max} = f(C_{pm\max}*)$ &$E_{\min} = f(C_{pm\min}*)$. (c) $E_{\max} = f(C_{pm\min}*)$ &$E_{\min} = f(C_{pm\mathrm{inflec}}*)$. (d) $E_{\max} = f(C_{pm\max}*)$ &$E_{\min} = f(C_{pm\mathrm{inflec}}*)$.

C. Maximum Misalignment Tolerance

From (4), if C_{pm} and C_{vm} vary due to plate misalignment, the resulting output voltage variation may exceed acceptable limits. Since the system gain is related to the compensation capacitors, the design of compensation parameters is crucial to ensuring the output voltage remains within the acceptable range under maximum plate misalignment.

To simplify the following theoretical analysis, normalized mutual capacitance $C_{pm}*$ and $C_{vm}*$ are defined as (18) to represent the system's tolerance to plate misalignment

$$\begin{cases} C_{vm}* = \frac{C_{vm}}{C_{vm\mathrm{coax}}} \\ C_{pm}* = \frac{C_{pm}}{C_{pm\mathrm{coax}}}. \end{cases} \tag{18}$$

where $C_{vm\mathrm{coax}}$ and $C_{pm\mathrm{coax}}$ are the mutual capacitances in well-aligned cases. Given that C_{pm} and C_{vm} of the coupler are approximately equal within the maximum misalignment tolerance, we have $C_{vm} = C_{pm}$. Then, $C_{vm}* = C_{pm}*$.

To simplify the calculations, λ and μ are defined as

$$\begin{cases} \lambda = \frac{C_{f\mathbf{2}}}{C_{vm\mathrm{coax}}} \\ \mu = \frac{C_{f\mathbf{1}}}{C_{pm\mathrm{coax}}}. \end{cases} \tag{19}$$

Substituting (18) and (19) into (4), the voltage gain can be derived as

$$E_t(C_{pm}*) = \frac{C_{pm}*}{\lambda} + \frac{\mu}{C_{pm}*}. \tag{20}$$

When the plates are not misaligned, the output voltage gain E_{req} is denoted as

$$E_{\boldsymbol{req}}(1 + \alpha) = \frac{1}{\lambda} + \mu. \tag{21}$$

An acceptable voltage range is defined as $V_o(1 \pm \alpha)$, where α, representing the allowable gain fluctuation, is typically set to 0.05 in practical applications [8]. To ensure output stability under misalignment, the system gain must remain within this range, Specifically, the system gain should not exceed the maximum threshold $E_{\max}$, nor fall below the minimum threshold $E_{\min}$. $E_{\max}$ and $E_{\min}$ are defined as

$$\begin{cases} E_{\max} \leq E_{\text{req}}(1+\alpha) \\ E_{\min} \geq E_{\text{req}}(1-\alpha). \end{cases} \tag{22}$$

The curve of E_t with respect to $C_{pm}*$ first decreases and then increases by (20). By setting the partial derivative of E_{t} concerning $C_{pm}*$ to zero, the inflection point $C_{pm\text{inflec}}*$ corresponding to the minimum gain is obtained as

$$C_{pm\text{inflec}}* = \sqrt{\lambda\mu}. \tag{23}$$

Based on the relationship between $C_{pm\text{inflec}}*$ and $[C_{pm\max}*, C_{pm\min}*]$, the E_t curve can be classified into two types with four cases, as shown in Fig. 9.

Type 1: $E_{\text{t}} = f(C_{pm}*)$ is monotonic in $[C_{pm\min}*, C_{pm\max}*]$.

1) If $E_t = f(C_{pm}*)$ is monotonically decreasing. The condition $C_{pm\text{inflec}}*\geq C_{pm\max}*$ holds, as shown in Fig. 9(a). Solving (21) and (23), we obtain

$$\lambda \geq \frac{C_{pm\max}*^2+1}{E_{\text{req}}(1+\alpha)}. \tag{24}$$

Meanwhile

$$\begin{cases} E_{\max} = f(C_{pm\text{coax}}*) \\ E_{\min} = f(C_{pm\max}*). \end{cases} \tag{25}$$

Solving (22) and (25), we have

$$\lambda \leq \frac{C_{pm\max}*^2-1}{[(1-\alpha)C_{pm\max}*-(1+\alpha)]E_{\text{req}}}. \tag{26}$$

λ can be determined using (24) and (26). If there is no cross section between (24) and (26), then $E_t = f(C_{pm}*)$ is not monotonically decreasing.

1) If $E_t = f(C_{pm}*)$ is monotonically increasing. The condition $C_{pm\text{inflec}}*\leq C_{pm\min}*$ holds, as shown in Fig. 9(b). Solving (21) and (23), we obtain

$$\lambda \leq \frac{C_{pm\min}*^2+1}{E_{\text{req}}(1+\alpha)}. \tag{27}$$

Meanwhile

$$\begin{cases} E_{\max} = f(C_{pm\text{coax}}*) \\ E_{\min} = f(C_{pm\min}*). \end{cases} \tag{28}$$

Solving (27) with (28), we obtain

$$\lambda \geq \frac{1-C_{pm\min}*^2}{[1+\alpha-(1-\alpha)C_{pm\min}*]E_{\text{req}}}. \tag{29}$$

Here, λ can be chosen using (27) and (29). If no intersection exists between (27) and (29), then $E = f(C_{pm}*)$ is not monotonically increasing.

Type 2: If $E_t = f(C_{pm}*)$ is not monotonic in $[C_{pm\min}*, C_{pm\max}*]$. Clearly, $E_{\min}$ occurs at the inflection point, $E_{\min} = f(C_{pm\text{inflec}}*)$. By substituting $E_{\min}$ into (22), we obtain

$$\frac{2(1-\sqrt{\alpha})^2}{(1-\alpha)^2E_{\text{req}}} \leq \lambda \leq \frac{2(1+\sqrt{\alpha})^2}{(1-\alpha)^2E_{\text{req}}}. \tag{30}$$

Since $C_{pm\text{coax}}*\leq C_{pm\text{inflec}}*\leq C_{pm\max}*$, we obtain

$$\frac{2}{E_{\text{req}}(1+\alpha)} \leq \lambda \leq \frac{C_{pm\max}*^2+1}{E_{\text{req}}(1+\alpha)}. \tag{31}$$

If $E_{\max}$ corresponds to $C_{pm\min}*$ as shown in Fig. 9(c), $E_{\max} = f(C_{pm\min}*)$ and $f(C_{pm\max}*) \leq E_{\text{req}}(1+\alpha)$. Solving (20) and (22), we obtain

$$\lambda \geq \frac{1+C_{pm\max}*}{E_{\text{req}}(1+\alpha)}. \tag{32}$$

Since $C_{pm\min}*\leq C_{pm\text{inflec}}*\leq C_{pm\text{coax}}*$, we obtain

$$\frac{C_{pm\min}*^2+1}{E_{\text{req}}(1+\alpha)} \leq \lambda \leq \frac{2}{E_{\text{req}}(1+\alpha)}. \tag{33}$$

If $E_{\max}$ corresponds to $C_{pm\max}*$ as shown in Fig. 9(d), $E_{\max} = f(C_{pm\max}*)$ and $f(C_{pm\min}*) \leq E_{\text{req}}(1+\alpha)$. Solving (20) and (22), we have

$$\lambda \leq \frac{C_{pm\min}*+1}{E_{\text{req}}(1+\alpha)}. \tag{34}$$

Here, λ can be chosen using (30), (31), (32), or (30), (33), (34). If no intersection exists, the allowable range for plate misalignment must be further constrained.

With the known λ, C_{f1} and C_{f2} can be obtained from (19) and (21). The compensation inductors L_1, L_2, L_3, L_4, L_{f1}, L_{f2} can be calculated by (2).

D. Design Procedure

The resonant angular frequency ω_0, voltage fluctuation range α, and geometric dimensions of the capacitive coupler are given based on the application requirement. The self-capacitances C_1, C_2, C_3, C_4 and mutual capacitances C_{pm}, C_{vm} of the capacitive coupler are obtained through FEA. To minimize voltage stress across the coupling plates, maximize system efficiency, and enhance misalignment tolerance, the voltage gain E_{req}, parallel capacitor C_{ex}, and compensation capacitor C_{f2} should be designed. First, E_{req} is determined by minimizing the voltage stress on the primary and secondary sides of the coupling plates. Subsequently, C_{ex} is optimized to achieve maximum system efficiency. Finally, C_{f2} is optimized to ensure the high misalignment tolerance. The detailed parameter design flowchart is shown in Fig. 10.

V. EXPERIMENTAL EVALUATION

To verify the above analysis, a hybrid electric field coupling CPT system has been built. The operating frequency is set as 1MHz. The input voltage is 100 V. The required output voltage is 170V. Using the design flowchart shown in Fig. 10, C_{f2} is calculated to be within [5.7 nF, 6.4 nF] and the E_t curve is not monotonic in the range of $[C_{pm\min}, C_{pm\max}]$ to satisfy the voltage fluctuation range in the *X*-axis misalignment, *Y*-axis misalignment and *Z*-axis misalignment. To facilitate zero-voltage switching (ZVS) of $Q_{1,23,4}$, L_{11} and L_{12} are slightly increased by the same value to achieve ZVS. An experiment prototype is constructed to verify the proposed system, which is shown in Fig. 11. The electric coupler and compensation parameters are given in Table I.

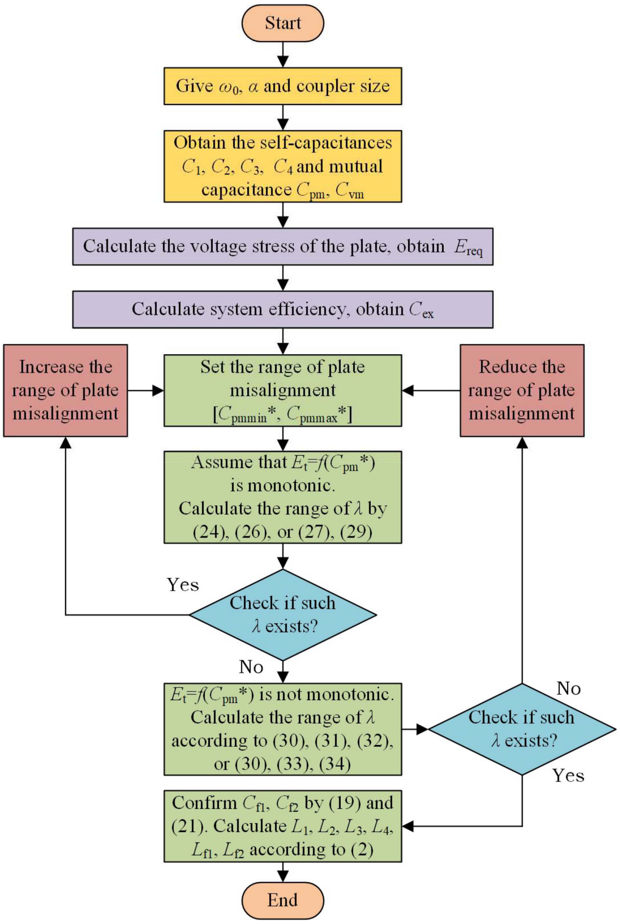

Fig. 10. Flowchart for parameter design.

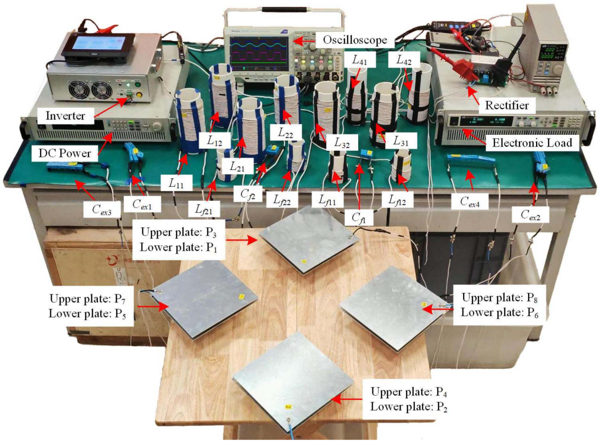

Fig. 11. Experimental prototype of the hybrid CPT system.

TABLE I

PARAMETERS OF PROTOTYPE HYBRID CPT SYSTEM

Parameters	Value	Parameters	Value
Frequency	1MHz	Input voltage	100 V
E_{req}	1.7	Output power	303 W
L_{11}, L_{12}	46.8 μH	L_{21}, L_{22}	48.5 μH
L_{31}, L_{32}	49.5 μH	L_{41}, L_{42}	46.3 μH
L_{f11}, L_{f12}	3.2 μH	L_{f21}, L_{f22}	2.2 μH
C_{f1}	4 nF	C_{f2}	5.7 nF
C_{ex1}, C_{ex2}	250 pF	C_{ex3}, C_{ex4}	250 pF
C_f	50.1 pF	C_1, C_2, C_3, C_4	273.6 pF
C_{vm}, C_{pm}	3.32 nF	k_1, k_2	0.0824

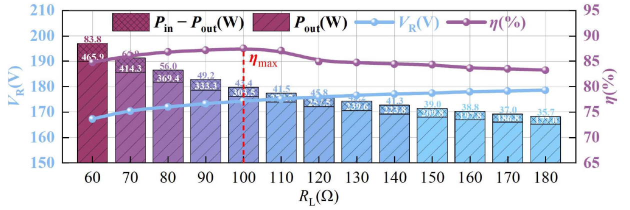

Fig. 12. Measured output voltage, efficiency, output power, and loss varying with R_L load.

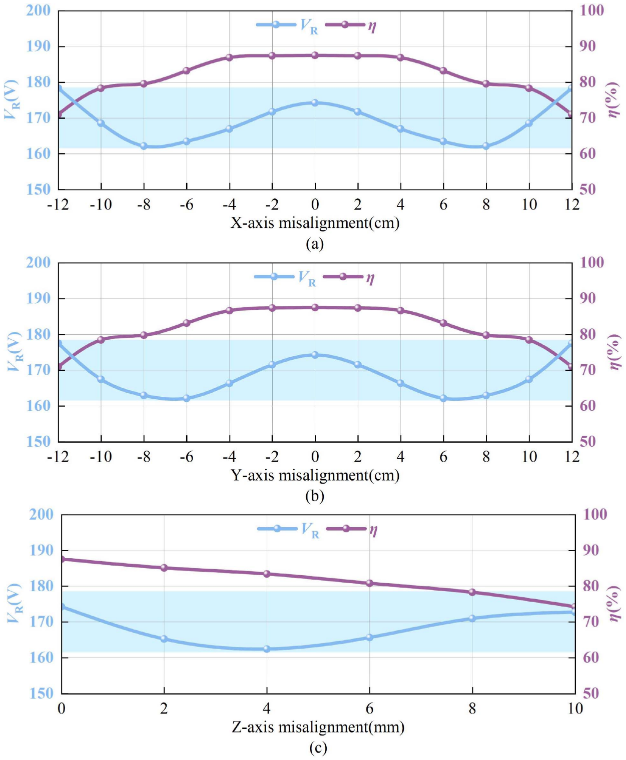

Fig. 13. Measured output voltage varying with (a) X-axis misalignment, (b) Y-axis misalignment, and (c) Z-axis misalignment.

Fig. 12 shows the measured output voltage, efficiency, output power and loss variation under different load resistances. As the load resistance R_L increases, the system efficiency exhibits noticeable variation, reaching a maximum efficiency at 100 Ω. Further validation on enhancing the system's tolerance to misalignment is based on this optimal condition. Fig. 13(a), (b), and (c) shows the measured output voltage variation under misalignment along X-axis, Y-axis, and Z-axis. It can be observed that the system maintains the output voltage with the predesigned 5% fluctuation range under a misalignment of 12-cm along the X-axis, 12-cm along Y-axis and 10-mm along the Z-axis. The X-axis and Y-axis misalignment are evaluated relative to the diagonal length of the plate, with the system achieving a

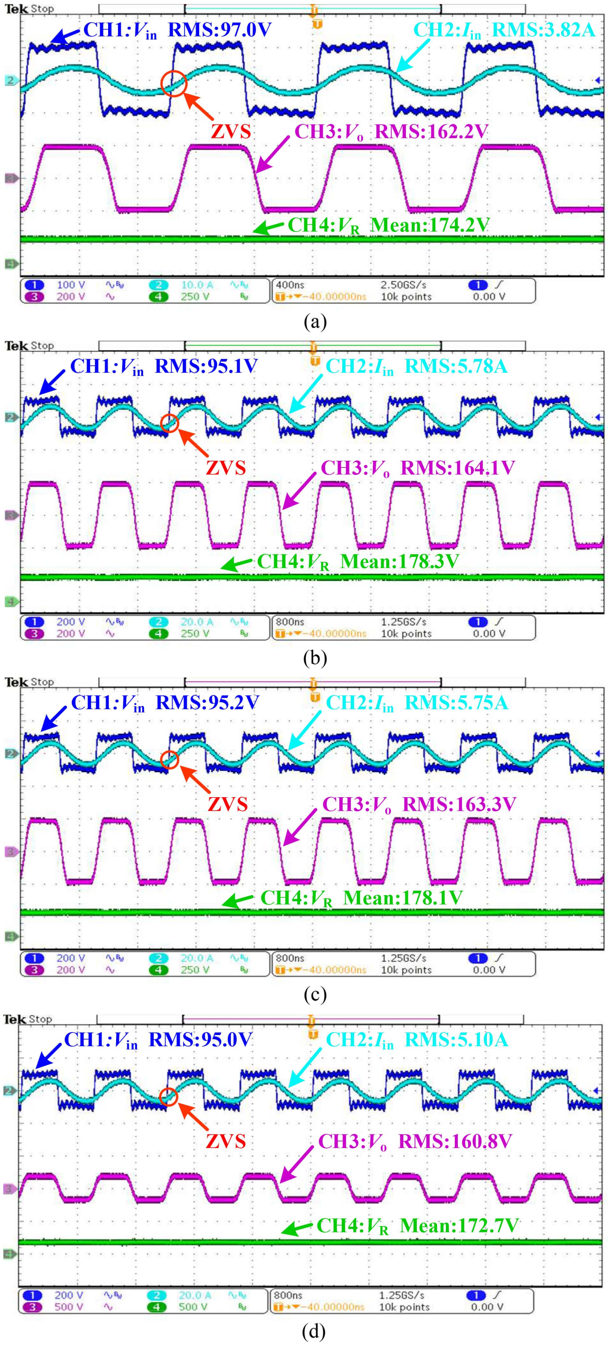

Fig. 14. Experimental waveforms of $V_{\rm in}$, $I_{\rm in}$, V_o, and V_R. (a) In well-aligned case. (b) At 12 cm *X*-axis misaligned position. (c) At 12 cm *Y*-axis misaligned position. (d) At 10 mm *Z*-axis misaligned position.

maximum lateral misalignment tolerance of 40%. The *Z*-axis misalignment is referenced to the transmission distance of the coupler, achieving a maximum tolerance of 100%. These results demonstrate the system's excellent tolerance to plate misalignment in all three dimensions.

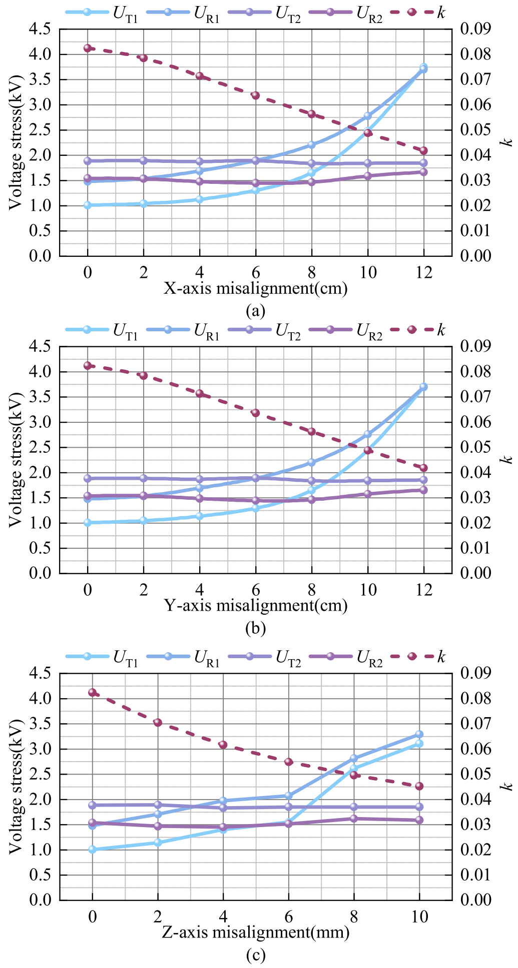

Fig. 15. Voltage stress and efficiency varying with (a) X-axis misalignment, (b) Y-axis misalignment, and (c) Z-axis misalignment.

Fig. 14(a) presents the experiment waveforms of $V_{\rm in}$, $I_{\rm in}$, V_o, V_R under the well-aligned case. Fig. 14(b), (c), and (d) displays the experimental waveforms in 12 cm *X*-axis misalignment, 12 cm *Y*-axis misalignment, and 10 mm *Z*-axis misalignment. It can be observed that the output voltage keeps almost 170 V although the lateral misalignment is tolerated to 40% of coupler length. Besides, there is a small phase angle of $I_{\rm in}$ lagging $V_{\rm in}$, which indicates ZVS realization of the full-bridge MOSFETs.

Fig. 15(a), (b) and (c) show the voltage stresses U_{T1}, U_{R1}, U_{T2}, U_{R2} and coupling coefficient *k* variation under misalignment along *X*-axis, *Y*-axis and *Z*-axis. Under misalignment conditions, the voltage stresses on the first power channel U_{T1} and U_{R1} increase rapidly as *k* decreases, while the voltage stresses on the second power channel U_{T2} and U_{R2} demonstrate significantly less variation, which is consistent with (10). The voltage stress is related to coupling coefficient. This inverse correlation between *k* and maximum voltage stress indicates that enhancing the coupling coefficient would reduce voltage stress in designs.

Fig. 16 shows the power loss distribution of the proposed hybrid CPT system. The power loss of all compensation inductors is calculated based on the impedance of coils of identical length measured using an LCR meter and the corresponding current. For the compensation capacitors, the loss is determined from the dissipation factor, capacitive reactance, and the voltage across each capacitor. The losses of the inverter and rectifier are estimated using experimentally measured values and parasitic

TABLE II
COMPARISONS OF CPT SYSTEM TOLERANCE TO PLATE MISALIGNMENT

Literatures	Qing et al. [7]	Qing et al. [12]	Luo et al. [13]	Cai et al. [4]	Li et al. [10]	Wei et al. [24]	Choi et al. [3]	This article
Method	Frequency tracking	Parameter design	Parameter design	Coupler design	Coupler design	Coupler design	Topology design	Topology design
Topology	*LC-LC*	*LC-LC*	*LC-CLC*	*LC-LC*	SS	*LC-LC*	*LCLCLC* (T-model)	*LCLC-LC* + *LC-LCLC*
Output model	CV/CC	CV	CP	CC	CC	CP	CP	CV
Misalignment	X-33% Z-100%	310-1470 pF	X-50% Y-50%	X/Y- [-10 cm,10 cm] θ- [0°,360°]	X-10% Y-10%	X-16%	Coupling variation-40%	X-40% Y-40% Z-100%
Frequency	1 MHz	600 kHz	600 kHz	500 kHz	2 MHz	1 MHz	1.30–1.45 MHz	1 MHz
Transmission distance	20 mm	Not mentioned	150 mm	Not mentioned	10 mm	60 mm	0.2 mm	10 mm
Efficiency	85%	85%	90.56%	82.5%	86.5%	87.2%	91.2%	87.5%
Fluctuation range	2%	8.3%	X-15.2% Y-10.6%	6.5%	3.5%	10%	5.8%	5%

TABLE III
COMPARISONS OF CPT SYSTEM VOLTAGE STRESS

Literatures	Zhang et al. [23]	Lu et al. [25]	Lian et al. [26]	Lian and Qu [27]	Wei et al. [28]	Chen et al. [29]	This article
Topology	Double-sided *LCL*	Double-sided *LCLC*	Double-sided *LCLC*	*LC-LC*	*LC-LCLC*	Double-sided *LCL*	*LCLC-LC* + *LC-LCLC*
Output model	CC	CC	CC	CC	CV	CC	CV
Misalignment	×	×	×	×	×	×	X-40% Y-40% Z-100%
Frequency	1 MHz	1 MHz	500 kHz	200 kHz	1 MHz	1 MHz	1 MHz
Transmission distance	150 mm	150 mm	6 mm	0.5 mm	250 mm	50 mm	10 mm
Primary plates voltage stress	5120 V	3200 V	1030 V	760 V	5 kV	1450 V	1005 V, 1883 V
Secondary plates voltage stress	5080 V	3200 V	985 V	730 V	5 kV	1450 V	1477 V, 1539 V
Power	1.87 kW	2.4 kW	40 W	60 W	2.2 kW	500 W	303 W
Efficiency	85.87%	90.8%	83%	Not mentioned	87.2%	90%	87.5%

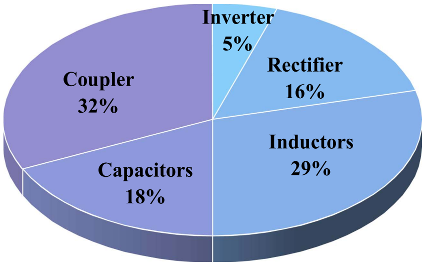

Fig. 16. Power loss distribution of the proposed CPT system.

parameters provided in the component datasheets. By subtracting the losses of the inverter and all compensation components from the total power loss—calculated from the measured system efficiency—the remaining loss is attributed to the capacitive coupler. Notably, compensation inductors and capacitors collectively accounted for 47% of the total power dissipation, constituting the predominant share among all loss components. This finding demonstrates significant power dissipation within the compensation network of the proposed system.

The performance of prior CPT systems regarding misalignment tolerance is given in Table II. It highlights key factors such as method, topology, output model, misalignment tolerance of different directions, operating frequency, transmission distance, efficiency, and fluctuation range. Compared with [7], [10], and [24], the proposed system achieves CV output within a wide misalignment range of 40% along the X- axis and Y-axis and 100% along the Z-axis. This indicates high misalignment tolerance. In addition, compared with [4], [12], [13], and [24], the voltage fluctuation remains within 5%, demonstrating improved output stability. Compared with [7], the proposed method does not require complex control strategies or additional power electronic devices, which indicates a promising outlook for future deployment. Compared with [3], which focuses solely on the variation of mutual capacitance, the proposed coupler operates at a relatively long transmission distance, and the proposed method evaluates the output performance under different directional misalignment, which is essential for practical CPT applications. These improvements clearly indicate enhanced misalignment tolerance and output stability compared with the recently literatures.

Different topologies have been proposed to achieve performance such output model, misalignment tolerance of different directions, frequency, transmission distance, primary plates voltage stress, secondary plates voltage stress, power, and efficiency. Comparison is given in Table III.

As given in Tables II and III, previous studies have focused solely on either misalignment tolerance or voltage stress. In contrast, this article simultaneously enhances misalignment tolerance while optimizing voltage stress and system efficiency, thereby providing practical guidance for future applications.

VI. CONCLUSION

This article proposes a new hybrid CPT system to enhance tolerance to plate misalignment and ensure CV output. The proposed system is configured to form an IPOS connection of the *LCLC-LC* and *LC-LCLC* compensation topologies. A novel QD-HCC is designed to achieve decoupling of misalignments along the *X*-axis, *Y*-axis, and *Z*-axis. Consequently, the two electric field coupling power transfer channels operate independently, effectively mitigating complex cross-coupling. Furthermore, a triple-effect multiobjective optimization method is proposed to jointly reduce plate voltage stress, enhance efficiency and improve misalignment tolerance. Experiment results shows that the proposed system achieves CV output for 40% *X*-axis misalignment, 40% *Y*-axis misalignment and 100% *Z*-axis misalignment within 5% output fluctuation with a maximum efficiency of 87.5%. These results indicate that the proposed system offers a promising solution for charging applications in cleaning robots that requiring high spatial flexibility.

REFERENCES

[1] K. Wang and S. Sanders, “Contactless USB—A capacitive power and bidirectional data transfer system,” in *Proc. IEEE Appl. Power Electron. Conf. Expo.*, 2014, pp. 1342–1347.

[2] B. Regensburger, J. Estrada, A. Kumar, S. Sinha, Z. Popović, and K. K. Afridi, “High-performance capacitive wireless power transfer system for electric vehicle charging with enhanced coupling plate design,” in *Proc. IEEE Energy Convers. Congr. Expo.*, 2018, pp. 2472–2477.

[3] S. Choi, E. Chung, G. C. Lim, J. S. Hong, G. Y. Choe, and J. I. Ha, “Single-sided compensation network design method for capacitive power transfer system considering coupling variation,” *IEEE Trans. Ind. Appl.*, vol. 60, no. 4, pp. 6351–6365, Jul./Aug. 2024.

[4] C. Cai, X. Liu, S. Wu, X. Chen, W. Chai, and S. Yang, “A misalignment tolerance and lightweight wireless charging system via reconfigurable capacitive coupling for un aerial vehicle applications,” *IEEE Trans. Power Electron.*, vol. 38, no. 1, pp. 22–26, Jan. 2023.

[5] K. Lu, S. K. Nguang, S. Ji, and L. Wei, “Design of auto frequency tuning capacitive power transfer system based on class-E^2 dc/dc converter,” *IET Power Electron.*, vol. 10, no. 12, pp. 1588–1595, Oct. 2017.

[6] Z. Xue, K. T. Chau, W. Liu, T. Yang, and T. W. Ching, “Pulse frequency modulation control for capacitive power transfer system with flexible output voltage,” in *Proc. IEEE Wireless Power Technol. Conf. Expo*, 2023, pp. 1–5.

[7] X. Qing, Y. Su, A. P. Hu, X. Dai, and Z. Liu, “Dual-loop control method for CPT system under coupling misalignments and load variations,” *IEEE J. Emerg. Sel. Topics Power Electron.*, vol. 10, no. 4, pp. 4902–4912, Aug. 2022.

[8] X. Qing, Z. Li, X. Wu, Z. Liu, L. Zhao, and Y. Su, “A hybrid wireless power transfer system with constant and enhanced current output against load variation and coupling misalignment,” *IEEE Trans. Power Electron.*, vol. 38, no. 10, pp. 13219–13230, Oct. 2023.

[9] J. Q. Zhu et al., “A novel capacitive coupler array with free-positioning feature for mobile tablet applications,” *IEEE Trans. Power Electron.*, vol. 34, no. 7, pp. 6014–6019, Jul. 2019.

[10] H. Li, Y. Liu, and M. Fu, “Circular capacitive coupler with multilayer interleaving for stable output,” *IEEE Trans. Microw. Theory Techn.*, vol. 71, no. 2, pp. 719–726, Feb. 2023.

[11] C. Liang et al., “An anti-offset CPT system with multiple pickups for mobile desktop application,” *IEEE Trans. Power Electron.*, vol. 39, no. 3, pp. 3826–3841, Mar. 2024.

[12] X. D. Qing, Z. H. Wang, Y. G. Su, Y. M. Zhao, and X. Y. Wu, “Parameter design method with constant output voltage characteristic for bilateral LC-compensated CPT system,” *IEEE J. Emerg. Sel. Topics Power Electron.*, vol. 8, no. 3, pp. 2707–2715, Sep. 2020.

[13] B. Luo, R. Mai, L. Guo, D. Wu, and Z. He, “LC-CLC compensation topology for capacitive power transfer system to improve misalignment performance,” *IET Power Electron.*, vol. 12, no. 10, pp. 2626–2633, Aug. 2019.

[14] G. Ke, Q. Chen, L. Xu, X. Ren, and Z. Zhang, “Analysis and optimization of a double-sided S-LCC hybrid converter for high misalignment tolerance,” *IEEE Trans. Ind. Electron.*, vol. 68, no. 6, pp. 4870–4881, Jun. 2021.

[15] L. Zhao, D. J. Thrimawithana, U. K. Madawala, A. P. Hu, and C. C. Mi, “A misalignment-tolerant series-hybrid wireless EV charging system with integrated magnetics,” *IEEE Trans. Power Electron.*, vol. 34, no. 2, pp. 1276–1285, Feb. 2019.

[16] X. Qu, Y. Yao, D. Wang, S.-C. Wong, and C. K. Tse, “A family of hybrid IPT topologies with near load-independent output and high tolerance to pad misalignment,” *IEEE Trans. Power Electron.*, vol. 35, no. 7, pp. 6867–6877, Jul. 2020.

[17] Y. Chen, B. Yang, Z. Kou, Z. He, G. Cao, and R. Mai, “Hybrid and reconfigurable IPT systems with high-misalignment tolerance for constant-current and constant-voltage battery charging,” *IEEE Trans. Power Electron.*, vol. 33, no. 10, pp. 8259–8269, Oct. 2018.

[18] L. Zhao, D. J. Thrimawithana, and U. K. Madawala, “Hybrid bidirectional wireless EV charging system tolerant to pad misalignment,” *IEEE Trans. Ind. Electron.*, vol. 64, no. 9, pp. 7079–7086, Sep. 2017.

[19] Y. Chen et al., “A hybrid inductive power transfer system with misalignment tolerance using quadruple-D quadrature pads,” *IEEE Trans. Power Electron.*, vol. 35, no. 6, pp. 6039–6049, Jun. 2020.

[20] T. Chen, C. Cheng, H. Cheng, C. Wang, and C. C. Mi, “Load-independent power-repeater capacitive power transfer system with multiple constant voltage outputs,” *IEEE J. Emerg. Sel. Topics Power Electron.*, vol. 10, no. 5, pp. 6358–6370, Oct. 2022.

[21] W. Zhou, Q. Gao, R. Mai, Z. He, and A. P. Hu, “Design and analysis of a CPT system with extendable pairs of electric field couplers,” *IEEE Trans. Power Electron.*, vol. 37, no. 6, pp. 7443–7455, Jun. 2022.

[22] S. Wang, J. Liang, and M. Fu, “Analysis and design of capacitive power transfer systems based on induced voltage source model,” *IEEE Trans. Power Electron.*, vol. 35, no. 10, pp. 10532–10541, Oct. 2020.

[23] H. Zhang, F. Lu, H. Hofmann, W. Liu, and C. C. Mi, “A four-plate compact capacitive coupler design and LCL-compensated topology for capacitive power transfer in electric vehicle charging application,” *IEEE Trans. Power Electron.*, vol. 31, no. 12, pp. 8541–8551, Dec. 2016.

[24] X. Wei, X. Shen, J. Jiang, S. Luo, Y. Zhu, and H. Ma, “An improved design method based on a multi-plate coupler structure for capacitive power transfer with wide ranges of misalignment and loads,” *IEEE J. Emerg. Sel. Topics Power Electron.*, vol. 12, no. 5, pp. 5311–5322, Oct. 2024.

[25] F. Lu, H. Zhang, H. Hofmann, and C. Mi, “A double-sided LCLC-compensated capacitive power transfer system for electric vehicle charging,” *IEEE Trans. Power Electron.*, vol. 30, no. 11, pp. 6011–6014, Nov. 2015.

[26] J. Lian, X. Qu, X. Chen, and C. C. Mi, “Design of a double-sided LCLC-compensated capacitive power transfer system with predesigned coupler plate voltage stresses,” *IEEE J. Emerg. Sel. Topics Power Electron.*, vol. 10, no. 1, pp. 128–137, Feb. 2022.

[27] J. Lian and X. Qu, “Design of a double-sided LC compensated capacitive power transfer system with capacitor voltage stress optimization,” *IEEE Trans. Circuits Syst. II: Exp. Briefs*, vol. 67, no. 4, pp. 715–719, Apr. 2020.

[28] X. Wei et al., “A circuit design method for constant voltage output with zero phase angle and minimum coupler voltages in capacitive power transfer,” *IEEE Trans. Power Electron.*, vol. 38, no. 3, pp. 4181–4192, Mar. 2023.

[29] T. Chen, C. Cheng, X. Zhang, G. Li, Y. Guo, and C. C. Mi, “A double-sided LCL-compensated network for the strongly coupled CPT system with minimum plate voltage stresses,” *IEEE J. Emerg. Sel. Topics Power Electron.*, vol. 12, no. 4, pp. 4275–4287, Aug. 2024.

Ting Chen received the B.S. degree in electrical engineering and automation, M.S. degree in control engineering, and Ph.D. degree in electrical engineering from the China University of Mining and Technology, Beijing, China, in 2015, 2017, and 2022, respectively.

From 2019 to 2021, she was a joint Ph.D. student with the Department of Electrical and Computer Engineering, San Diego State University, San Diego, CA, USA. She is currently an Associate Professor with the Department of Electrical Engineering and State Key Laboratory of Intelligent Power Distribution Equipment and System, Hebei University of Technology, Tianjin, China. Her current research interests include wireless power transfer technologies, modeling and control of switching converters.

Zhihui Ma received the B.S. degree in electrical engineering and automation from Shijiazhuang Tiedao University, Shijiazhuang, China, in 2021. He is currently working toward the M.E. degree in electrical engineering with the Hebei University of Technology, Tianjin, China.

His research interests include engineering electromagnetism, wireless power transfer, and its industrial applications.

Zhicheng Xu received the Ph.D. degree in engineering from Southeast University, Nanjing, China, in 2022.

He is currently an Associate Professor, a Doctoral Supervisor, and the Deputy Director with the Department of Smart Energy at the School of Electrical Engineering, Hebei University of Technology, Tianjin China. He has presided more one National Natural Science Foundation of China project and one sub-project of the National Key R&D Program of China. His main research interests include operation and maintenance management and control of electrochemical energy storage systems, and wireless intelligent sensors.

Fengxian Wang received the B.S. degree in electrical engineering and the M.S. degree in electrical engineering from Tiangong University, Tianjin, China, in 2018 and 2021, respectively. He is currently working toward the Ph.D. degree in electrical engineering with the Hebei University of Technology, Tianjin, China.

His research interests include engineering electromagnetism, wireless power transfer, and its industrial applications.

Xian Zhang received the M.E. and Ph.D. degrees in electrical engineering from the Hebei University of Technology, Tianjin, China, in 2009, and 2012, respectively.

He is currently a Professor with the Hebei University of Technology, Tianjin, China. He is the Director of the China Electrotechnical Society and the secretary-general of the National Specialized Committee on Wireless Power Transmission Technology. His research interests encompass intelligent high-power wireless power transmission technology, measurement of three-dimensional electromagnetic fields, and numerical calculations of modern engineering electromagnetic fields.

Guangyao Li received the B.S. degree in electronic engineering from the Tianjin Sino-German University of Applied Sciences, Tianjin, China, in 2022. He is currently working toward the M.E. degree in electrical engineering with the Hebei University of Technology, Tianjin, China.

His research interests include engineering electromagnetism, wireless power transfer, and its industrial applications.

Xuan Zhao received the B.S. degree in electrical engineering and the M.S. degree in electrical engineering and automation in 2018 and 2022, respectively, from Hebei University of Technology, Tianjin, China, where he is currently working toward the Ph.D. degree in electrical engineering.

His research interests include engineering electromagnetism, wireless power transfer, and its industrial applications.

Yuqiao Wang received the B.S. degree in electrical engineering and automation in 2023 from the School of Electrical Engineering, Hebei University of Technology, Tianjin, China, where he is currently working toward the M.E. degree in electrical engineering.

His research interests include engineering electromagnetism, wireless power transfer, and its industrial applications.